Effect of Quencher, Geometry, and Light Outcoupling on the Determination of Exciton Diffusion Length in Nonfullerene Acceptors

Valentina Belova,* Aleksandr Perevedentsev, Julien Gorenflot,* Catherine S. P. De Castro, Miquel Casademont-Viñas, Sri H. K. Paleti, Safakath Karuthedath, Derya Baran, Frédéric Laquai, and Mariano Campoy-Quiles*

The correct determination of the exciton diffusion length (L_D) in novel organic photovoltaics (OPV) materials is an important, albeit challenging, task required to understand these systems. Herein, a high-throughput approach to probe L_D in nonfullerene acceptors (NFAs) is reported, that builds upon the conventional photoluminescence (PL) surface quenching method using NFA layers with a graded thickness variation in combination with spectroscopic PL mapping. The method is explored for two archetypal NFAs, namely, ITIC and IT-4F, using PEDOT:PSS and the donor polymer PM6 as two distinct and practically relevant quencher materials. Interestingly, conventional analysis of quenching efficiency as a function of acceptor layer thickness results in a threefold difference in L_D values depending on the specific quencher. This discrepancy can be reconciled by accounting for the differences in light in- and outcoupling efficiency for different multilayer architectures. In particular, it is shown that the analysis of glass/acceptor/PM6 structures results in a major overestimation of L_D, whereas glass/acceptor/PEDOT:PSS structures give no significant contribution to outcoupling, yielding L_D values of 6−12 and 8−18 nm for ITIC and IT-4F, respectively. Hence, practical guidelines for quencher choice, sample geometries, and analysis approach for the accurate assessment of L_D are provided.

V. Belova, A. Perevedentsev, M. Casademont-Viñas, M. Campoy-Quiles
Nanopto Group, Nanostructured Materials for Optoelectronics and Energy Harvesting Research Unit
Material Science Institute of Barcelona, ICMAB-CSIC
08193 Bellaterra, Spain
E-mail: valentina.belova@esrf.fr; mcampoy@icmab.es

J. Gorenflot, C. S. P. De Castro, S. H. K. Paleti, S. Karuthedath, D. Baran, F. Laquai
KAUST Solar Center (KSC)
Physical Sciences and Engineering Division (PSE)
Materials Science and Engineering Program (MSE)
King Abdullah University of Science and Technology (KAUST)
Thuwal 23955-6900, Kingdom of Saudi Arabia
E-mail: julien.gorenflot@kaust.edu.sa

1. Introduction

The field of solution-processed organic photovoltaics (OPV) has been experiencing renewed interest since the introduction of high-performance small-molecular nonfullerene acceptors (NFAs).[1–4] Solar cell efficiencies approaching 18% have, indeed, been reported when using these materials in single-junction devices.[4,5] To understand what makes the NFA family so special, a significant interest in their photophysical properties has been sparked.[6–9] One key material characteristic that has been claimed to play an all-important role is the large exciton diffusion length, L_D, reported for these systems compared with fullerene-based acceptors.[6,8,10] L_D, representing an average distance that an exciton can travel within its lifetime τ, describes the exciton migration in material and, therewith, determines the acceptable length scales of phase separation in bulk heterojunction (BHJ)-based solar cells.[11–15]

In contrast to other primary characteristics of OPV materials, such as energy levels, optical absorption, or even device performance, L_D cannot be quantified directly. For the past few decades, several approaches to evaluating L_D in organic semiconductors have been developed.[16,17] The most common methods are based on PL quenching analysis, including thickness-dependent (steady state[11,16,18–24] and time resolved (TR)[9,16,25–27]) and spectrally resolved[28,29] surface quenching and volume quenching,[6,16,30–32] electro-optical measurements,[8,22,26,33–37] exciton−exciton annihilation,[6–8,16,25,27] etc. All these techniques are based on rather complex models, where some parameters are derived using various approximations and simplifications. This inevitably leads to a significant underestimation of a number of contributing effects related to film roughness and morphology, as well as the distribution and interference of the electric field, to name but a few. Table S1, Supporting Information (SI) illustrates the widespread reported L_D values for a selection of common OPV materials obtained by different groups and methods. For instance, L_D in ITIC, one of the

archetypal NFAs, and its fluorinated derivative IT-4F, was recently analyzed by applying TR spectroscopy and exciton–exciton annihilation methods, resulting in roughly twofold discrepancy in the obtained values (18 ± 2 and 31.9 ± 0.7 nm for ITIC and 19 ± 2 and 47.4 ± 0.9 nm for IT–4F, respectively).[6,8]

In the present work, we focus on the PL surface quenching method, first proposed by Simpson in his pioneering work.[18] It provides a straightforward means to quantify L_D by fitting the quenching efficiency (QE) as a function of the active layer thickness (d) with a 1D exciton diffusion model and thus it remains one of the most direct ways to determine L_D.[18–20] A considerable downside of this method is that it is particularly fabrication- and process-demanding. Specifically, a systematic and consistent study of L_D in a given material requires a large series of reproducible half-covered bilayer (BL) samples with a wide thickness variation of the layers of interest and sharp, well-defined interfaces. Here, we establish a combined fabrication/measurement approach that overcomes the limitations of the standard thickness-dependent surface PL quenching method to thoroughly study singlet exciton diffusion in two widely used NFAs: ITIC, a benchmark small-molecule NFA, and its fluorinated derivative, IT–4F (**Figure 1**a). Variable-speed blade coating is used to produce acceptor thickness gradients that range from 10 to >100 nm within a single sample. The lateral gradients were implemented previously for the optimization and boosting acceleration of the

multiparametric screening of solution-processed solar cells.[38,39] Here, the thickness gradients are applied for the first time for the fast QE versus thickness data acquisition (up to several hundred data points can be collected from a few samples, increasing the self-consistency and statistical relevance of the method).

Another major problem arises for all analysis methods based on the interpretation of light emission from multilayer samples. Recent work demonstrated that the detected and intrinsic luminescence spectra can vary drastically due to variations in optical outcoupling, leading to a significant misinterpretation of the results.[40] As NFAs have high refractive indices,[41,42] we expect large fractions of PL emission to be trapped within the film through total internal reflection, thus leading to limited outcoupling efficiency. To investigate this aspect, we use two types of PL quenchers with very different optical properties (Figure 1b and Figure S1, Supporting Information), namely, a doped conductive polymer PEDOT:PSS and a wide-bandgap-conjugated push−pull polymer PM6 (alternatively termed elsewhere as "PBDB-T-2F"). They have similar work function/ionization energy levels, considered beneficial for hole transfer when paired with ITIC and IT–4F (Figure 1c and Figure S2, Supporting Information). PEDOT:PSS is widely known for its application as a hole-transport layer (HTL) in OPV and its ability to quench excitons was reported previously.[43–45] Importantly, water-processed PEDOT:PSS films are resistant to common organic solvents
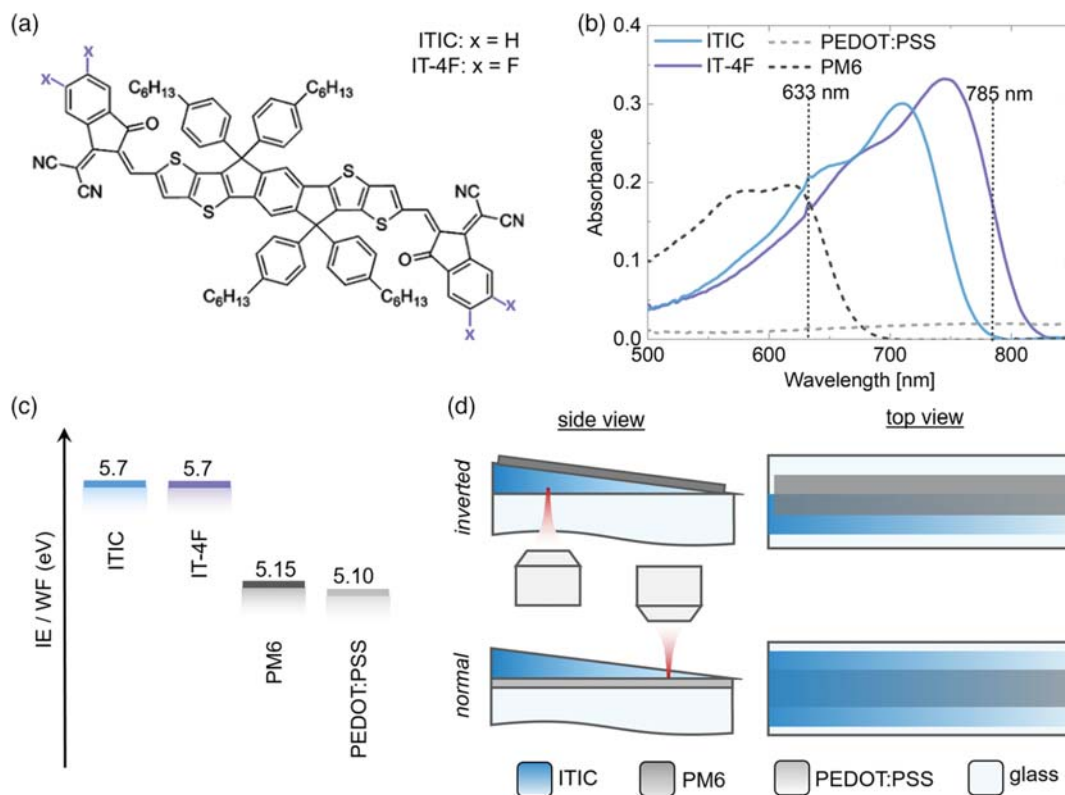
Figure 1. a) Chemical structure of ITIC and IT-4F. b) Optical absorption spectra of thin films (thickness d as indicated) of the acceptors: ITIC ($d = 20$ nm) and IT-4F ($d = 20$ nm) and donors/quenchers: PEDOT:PSS ($d = 10$ nm) and PM6 ($d = 25$ nm). Vertical markers indicate the excitation wavelengths used in subsequent analysis. c) Ionization energies (ITIC, IT-4F, PM6) and work function (PEDOT:PSS) were measured by PESA. d) Schematic of sample architectures and measurement geometries: ITIC/PM6 with the quencher atop the acceptor gradient measured in an "inverted" geometry (i.e., excitation and PL detection through the substrate); ITIC/PEDOT:PSS with the quencher underneath the acceptor gradient measured in a "normal" geometry.

and therefore ideally suited for subsequent deposition of NFA thickness gradients, ensuring the sharp interface needed for the PL surface quenching method. In the case of PM6, high-performance solar cells based on its combinations with both ITIC and IT–4F were recently demonstrated, evidencing a fairly efficient hole transfer from the NFAs.[46,47] The issue of local interdiffusion between ITIC and PM6 induced by swelling or partial dissolution during sequential solution-based film deposition due to comparable solubility of PM6 and NFAs in common solvents was overcome by implementation of a "floating transfer" method described in the following sections. The choice of the quenchers is also motivated by the need to minimize the overlap between the optical absorption spectra of the NFAs. By applying two excitation wavelengths, namely 633 and 785 nm (Figure 1b), we can evaluate the effect of absorption by the quencher as well as the effect of different absorption profiles: in the case of PEDOT:PSS quencher, the only change is the absorption profile across the sample stack, while in the case of PM6, there is an additional absorption by the quencher. The sample and measurement geometries with two quenchers are illustrated in Figure 1d.

The subsequent analysis uses 2D PL scanning to accurately extract the QE as a function of NFA layer thickness, with the results fitted using an exciton diffusion model to obtain L_D. We then calculate the degree of light outcoupling for both systems using a scattering matrix approach and apply the correction to the experimental QE data. The outcoupling contribution is found to be negligible in the case of PEDOT:PSS but plays a major role in the determination of the L_D for samples based on the PM6 quencher. We demonstrate that the light outcoupling issue persists for a wide range of optical constants, thicknesses, and different sample architectures. Overall, this study provides a comprehensive exploration of a versatile method for determining the exciton diffusion length for a variety of organic semiconductor materials in different sample geometries.

2. Results and Discussion

2.1. Sample Fabrication

The most direct approach to fabricating donor/acceptor bilayers (BLs) involves sequential solution-based deposition of the individual thin-film layers, although a major concern arises over concomitant redissolution of an underlying layer, which, therewith, would yield partially interdiffused BLs. A recent report[9] disclosed a method of obtaining ITIC/PM6 BLs via deposition of ITIC onto PM6 from solutions in dichloromethane, a substantially poor solvent for the latter. While coarse interdiffusion was conclusively ruled out, short-range intermixing of the two materials nevertheless remains likely in view of non-negligible simultaneous swelling of PM6 that may be expected for the halogenated solvent used in the subsequent deposition of the acceptor layer. Hence, to obtain ITIC/PM6 BLs with a maximally sharp interface, a "floating transfer" method was used in this study (see Experimental Section and Figure S3, Supporting Information). ITIC/PEDOT:PSS BLs were fabricated by the conventional sequential deposition given the insolubility of PEDOT:PSS in common organic solvents. In both cases, thickness gradients of the NFA were obtained by continuously varying

blade-coating deposition speed, yielding acceptor films with thicknesses spanning ≈10–120 nm within a single substrate.[38,39] The fabrication steps and parameters are provided in Experimental Section. The corresponding sample architectures are schematically illustrated in Figure 1d.

2.2. QE Analysis

In this work, we study L_D using and optimizing a well-established thickness-dependent surface PL quenching method, where a fraction of excitons generated in the layer of interest gets quenched at the interface with a quencher material.[18–20] The probability of a quenching event is in direct correlation with the distance between the photon absorption site and the interface. A larger fraction of excitons is more likely to reach the interface for layer thicknesses below L_D. The way to quantify the quenched exciton fraction is a direct comparison of the integrated PL intensity recorded from the active layer of a given thickness in the presence and absence of the quencher.

Here, using layers with thickness gradients partly covered with a quencher, we are able to collect reproducible and consistent data from a single sample, as illustrated in Figure 1d and **Figure 2**.[39] Exemplary PL spectra from thinner and thicker parts of ITIC gradients are shown in comparison with the corresponding BL spectra for two geometries, that is, 1) a quencher (PM6) deposited on top of an ITIC gradient (Figure 2a) and 2) a quencher (PEDOT:PSS) sandwiched between a substrate and an ITIC gradient (Figure 2b). In the former case, samples were excited through the glass ("inverted" imaging geometry, Figure 1d), whereas in the latter case, samples were excited from the top layer ("normal" imaging geometry, Figure 1d). PL maps were acquired with large-area scans with a size of 20 × 46 mm and a resolution of 250−500 μm pixel^{-1} (insets in Figure 2). The length of the gradient area is typically around 6 cm on the standard glass slide (7.5 cm long); therefore, for some samples, the mapping was done with two large-area scans. Practically, from a single sample, we obtained up to 240 datapoints from different NFA thicknesses that would otherwise require as many different samples. In addition, thanks to the reduced area of each probed pixel, any local defects which might appear during fabrication can be safely excluded at the data analysis stage. We note that the variation of NFA thickness within the pixel size is smaller than 1 nm. The resulting PL images contain well-defined areas across the scan long axis: ITIC and PM6 single layers and their overlap in the middle (marked as "BL") for the first geometry; ITIC with PEDOT:PSS underneath ("BL"); and ITIC single layer for the second geometry.

As expected, the PL intensity measured in the BLs is reduced strongly in the thinner part of the gradients. In Figure 2a, a weak contribution from PM6 to the BL PL signal can be seen as a shoulder between 640 and 720 nm, in particular for ITIC (20 nm)/PM6. To minimize the contribution of the donor to the data analysis, its signal was subtracted proportionally from the BL-integrated intensities along the full gradient. As the optical absorption of the PEDOT:PSS layer at the excitation wavelengths applied is considerably lower than that of the ITIC acceptors (Figure 1b), its contribution to the BL PL in ITIC/PEDOT:PSS heterostructures can be neglected (Figure 2b).
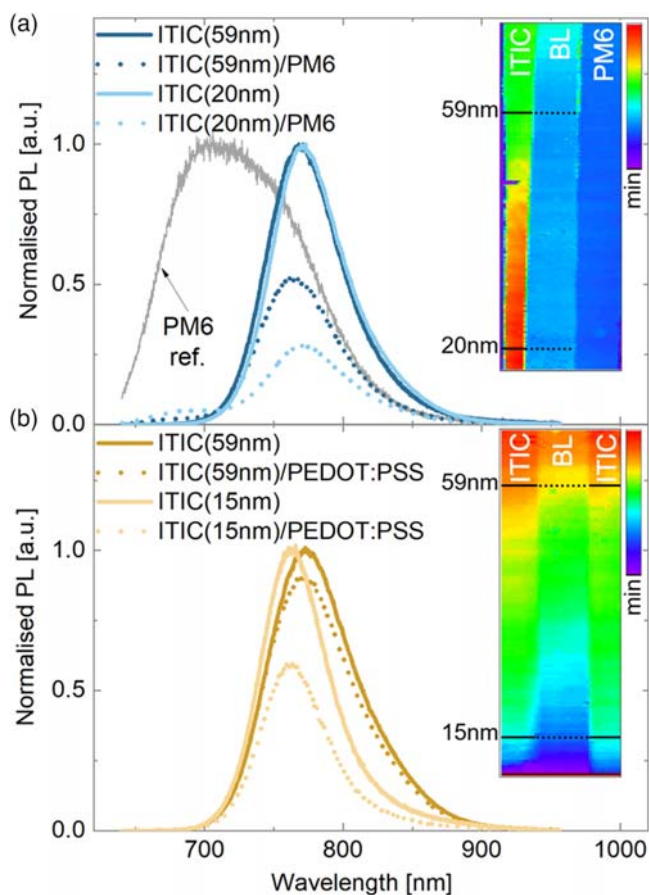
Figure 2. Exemplary PL emission spectra (633 nm excitation wavelength) of ITIC gradients shown: with a) PM6 (inverted measurement geometry) and b) PEDOT:PSS (normal measurement geometry) as quenchers. In both cases, steady-state PL of two thicknesses is provided. The solid and dotted lines correspond to spectra recorded at the ITIC-only and BL regions, respectively, at the particular ITIC thicknesses d (thicker and thinner parts of the gradients). PL data at each thickness are normalized by the maximum PL intensity for the ITIC-only sample region. The insets show the PL images acquired for the corresponding types of samples (thickness of the ITIC gradient decreases from top to bottom).

The PL of ITIC (PL_{ITIC}) and BL (PL_{BL}) was integrated across the corresponding areas for each scan line with an assigned thickness of the ITIC gradient d. Thus, the thickness-dependent QE is defined as

$$QE^{exp}(d) = 1 - \frac{PL_{BL}(d)}{PL_{ITIC}(d)} \tag{1}$$

and can vary between 1 (complete quenching) and 0 (no quenching).

The experimental PL quenching values versus gradient thickness acquired from multiple samples at 633 and 785 nm excitations for both NFAs are shown in **Figure 3** (scatter plots). Each graph contains two datasets for both sample geometries with PM6 and PEDOT:PSS as quenchers. The first thing to point out is that with our proposed method based on gradients, we can generate hundreds of data points of equivalent different

thicknesses, all within a single substrate. This is a great advantage over conventional methods. In contrast, the shape of the QE versus thickness plot is similar for the two NFA materials but strongly different depending on the quencher and geometry used.

The experimental approach for the determination of exciton diffusion parameters in organic semiconductors by the so-called direct observation was first designed by Simpson.[18] In the framework of the random walk concept, the mathematical analysis of exciton migration across a thin film (x-direction is normal to the film plane) was based on the 1D continuum diffusion equation.

$$\frac{\partial p(x,t)}{\partial t} = D \frac{\partial^2 p(x,t)}{\partial x^2} - \frac{p(x,t)}{\tau} + G(x,t) \tag{2}$$

where p is the temporally and spatially dependent exciton population, the first term on the right represents diffusion with the diffusion coefficient D, and the second and third terms are the exciton recombination and photogeneration. In steady-state conditions, the term on the left can be omitted and, taking into account that $L_D = \sqrt{D\tau}$, Equation (2) can be simplified to

$$L_D^2 \frac{\partial^2 p(x)}{\partial x^2} - p(x) + \tau G(x) = 0 \tag{3}$$

The exciton generation profile $G(x)$ is often described with an exponential decay in accordance with the Beer–Lambert law for the absorbed light. However, in the case of very thin films with thicknesses smaller in comparison with the incident wavelength λ and the extinction depth α^{-1}, possible interference effects due to reflection from the interfaces have to be taken into account. As $G(x)$ is proportional to the optical electric field intensity $|E(x)|^2$, the transfer matrix approach introduced by Pettersson et al.[33] and adapted by Burkhard et al.[48] can be applied for the calculation. **Figure 4** shows examples for the calculated distribution of the electric field intensity $|E(x)|^2$ within a stack for different geometries calculated for 60 nm-thick NFA layers. Here one can see that the different excitation wavelengths lead to different excitation profiles: 633 nm is quickly absorbed and 785 nm is redistributed through the bulk due to its weaker absorption. One can also notice differences in the PL quenching data in Figure 3 between two excitation wavelengths. However, as the $G(x)$ term, accounting for these differences, is included into the fitting model, the resulting L_D values are in principle independent of the excitation wavelength when the absorption profile is known and no energy transfer takes place.

Each sample studied can be considered as a combination of two-layered systems: without quenching interfaces (glass/NFA/air or air/NFA/glass for the inverted and normal imaging geometries, respectively) and with one quenching interface (glass/NFA/quencher/air or air/NFA/quencher/glass). Thus for these cases, further denoted as "nQ" and "Q" respectively, two systems of boundary conditions can be imposed.

$$\left. \frac{\partial p_{nQ}}{\partial x} \right|_{x=0} = 0, \quad \left. \frac{\partial p_{nQ}}{\partial x} \right|_{x=d} = 0 \tag{4}$$

and
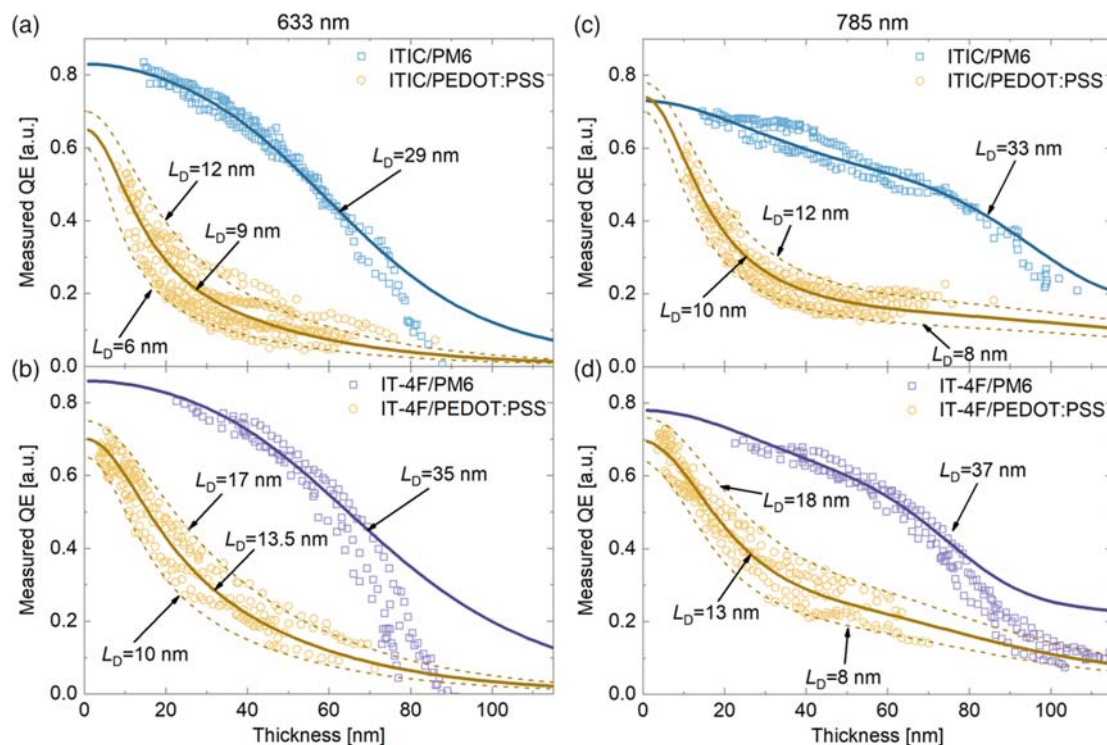
Figure 3. Measured (scatter plot) and modeled (solid and dashed curves) QE for a,b) 633 nm and c,d) 785 nm excitation in ITIC and IT–4F bilayers as a function of the emitter thickness and quencher with the corresponding L_D. Only every third data point is shown for clarity.
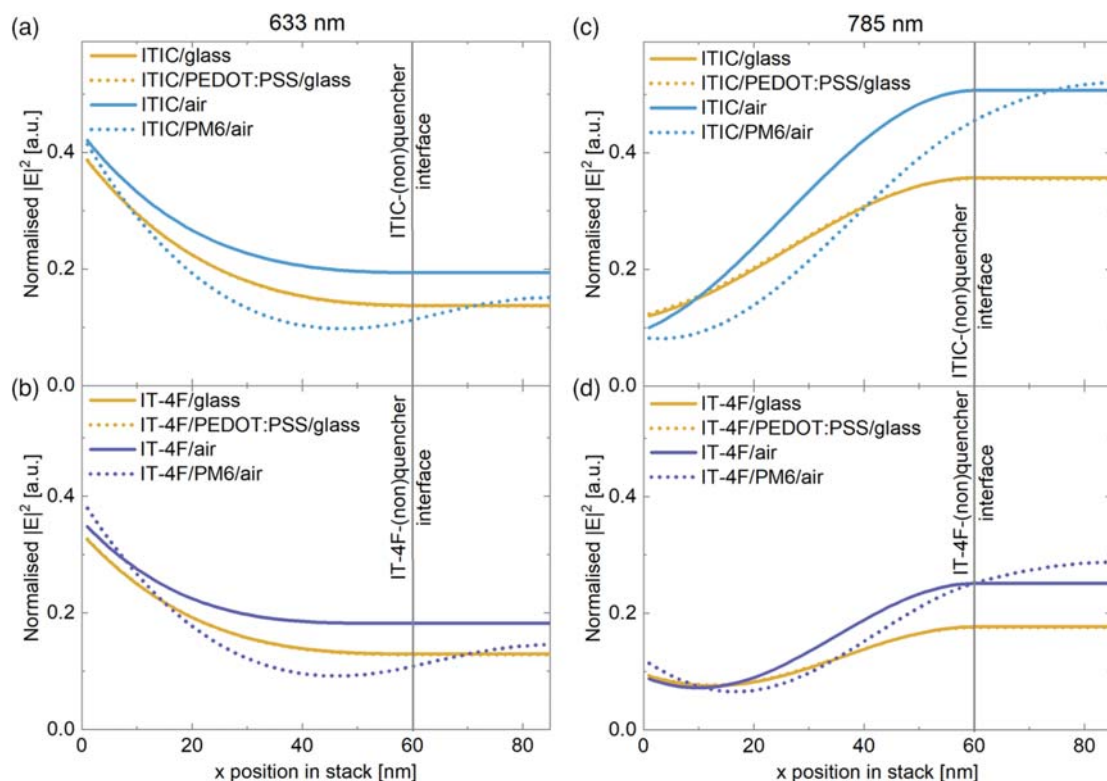
Figure 4. Distribution of the optical electric field intensity $|E(x)|^2$ within a stack for different geometries at a,b) 633 nm and c,d) 785 nm excitations: air/NFA(60 nm)/glass (solid orange), air/NFA(60 nm)/PEDOT:PSS(10 nm)/glass (dotted orange), glass/NFA(60 nm)/air (solid blue or purple), and glass/NFA(60 nm)/PM6(25 nm)/air (dotted blue or purple). Zero of the horizontal axis set to the illuminated interface of the NFAs.

$$\left.\frac{\partial p_Q}{\partial x}\right|_{x=0} = 0, \quad \left. p_Q \right|_{x=d} = 0 \tag{5}$$

The first three conditions are based on an assumption that there is no exciton transport across the nonquenching interfaces with glass or air and the last one implies a complete absorption of excitons by a quencher.

The system of Equation (3)−(5) was solved numerically by applying the finite-difference method with the implicit scheme. L_D can be estimated by fitting the resulting expression for the modeled QE

$$QE^{model} = 1 - V \frac{\int_0^d p_Q(x)\mathrm{d}x}{\int_0^d p_{nQ}(x)\mathrm{d}x} \tag{6}$$

to the experimental QE values from Equation (1). The parameter V was introduced to express a "quenching quality" or, namely, a portion of excitons reaching the interface that gets quenched (between 0 and 1) in accordance with Topczak et al.[24]

Using this framework, we can fit the data in Figure 3. The solid lines represent the QE simulations based on an assumption for the best-fit L_D and V values from the comparison with the experimental data. The dotted lines are provided to account for possible variations of the modeled QE profiles. The remarkable effect of the quencher/geometry can be seen for both NFAs. The gradients coupled with PM6 exhibit noticeably higher QE and as a result circa three times larger L_D values than those coupled with PEDOT:PSS; respectively: ≈29−33 nm versus 6−12 nm for ITIC and ≈35−37 nm versus 8−18 nm for IT–4F.

To verify that this difference does not arise from completely different quenching capabilities of both materials, we carried out photoelectron spectroscopy in air (PESA) to determine the ionization energies (ITIC, IT-4F, PM6) and work function (PEDOT:PSS) of the materials used (Figure S2, Supporting Information). According to the PESA results, the interesting energy levels of the two quenchers are very close, and both should lead to a high QE for an exciton arriving at the interface. In other words, both PM6 and PEDOT:PSS should exhibit a large enough driving force for charge transfer.

Moreover, we also believe that the differences are not due to a lack of sharpness of the interface, as we have produced clean bilayers using either orthogonal solvents or a transferring method. If an NFA/quencher interface is not sharp and an interdiffusion between the compounds takes place, it will lead to a quenching enhancement and, as a consequence, an overestimation of L_D. To further investigate this point, we have taken an ITIC/PM6 sample and measured the QE as a function of thermal annealing. The details are described in the Supporting Information. As shown in Figure S4, Supporting Information, we can clearly see that, provided that the temperature is kept below 100 °C, the quenching profile is kept the same, suggesting that molecular diffusion is only allowed at high temperatures (above the polymer glass transition). Based on this result, we can rule out the processing-related interface characteristics as the main reasons for the observed difference in the QE curves between the PEDOT:PSS- ($QE_{PEDOT:PSS}$) and PM6-based (QE_{PM6}) systems. We have also determined the surface roughness R_q over large areas (Figure S5, Supporting Information)

and noticed that the R_q for the ITIC layer (around 2−3 nm) is not different enough to explain the differences in the QE between the quenchers/geometries or its evolution with the NFA thicknesses.

2.3. Effect of Light In- and Outcoupling

Similar to the electric field intensity of the excitation light (see Figure 4), the light emitted from the device is strongly affected by the wavelength-dependent constructive or destructive interferences caused by the multilayer structure, to the point where the detected light can strongly differ from what is intrinsically emitted by the NFA layer (see, e.g., the clear spectral shift in Figure 2b). This has been shown, for example, in electroluminescence from organic solar cells by List et al.[40]

To account for optical coupling effects, we simulated those for the four considered device structures: air/glass/emitter/air, air/glass/emitter/quencher(PM6)/air, air/emitter/glass/air, and air/emitter/quencher(PEDOT:PSS)/glass/air. Absorption profile and emission outcoupling were calculated using the software Setfos 5.0 from Fluxim. The reflectance and transmission at the different interfaces of the multilayer structure are calculated using transfer matrix formalism, as described by Yeh,[49] based on the wavelength-dependent complex refractive indexes extracted by ellipsometry (Figure S1, Supporting Information).

In practice, we simulated the absorption profile of the excitation wavelength (633 or 785 nm) through different layers (proportional to the optical field density, see Figure 4). We then considered an absorption-coupled emission in which the distribution of emitting dipoles through the emitting layer has the same shape as the absorption profile (more details in the Supporting Information, Section 7). To identify the spectral distortion and intensity losses due to outcoupling, we simulated a uniform white light emission $PL_{WL}(\lambda)$, meaning that an emitting dipole could produce a photon with an equal probability for each wavelength within a chosen emission range. As shown in **Figure 5**, although the simulated emissive layer intrinsically emits a uniform spectrum, the detected spectra would strongly depend on the device structure, the quencher, and the thickness of the emitter.

We define the apparent quenching as the ratio of the simulated emissions with and without the quenching layer but without considering its quenching effect, that is, considering only the differences of in- and outcoupling

$$QE^{apparent} = 1 - \frac{PL_{simulated,quencher}(\lambda)}{PL_{simulated,no\,quencher}(\lambda)} \tag{7}$$

As in Figure 5, for the case of PEDOT:PSS quencher and device structure, $PL_{simulated}(\lambda)$ is almost identical with (d) and without the quencher (b). In fact, spectrally integrating this apparent quenching shows that the difference in the optical coupling should not generate more than a 1.5% difference between the emission with and without a quencher. This value is in the range of the experimental error and reached only for the most extreme thicknesses. It is thus not necessary
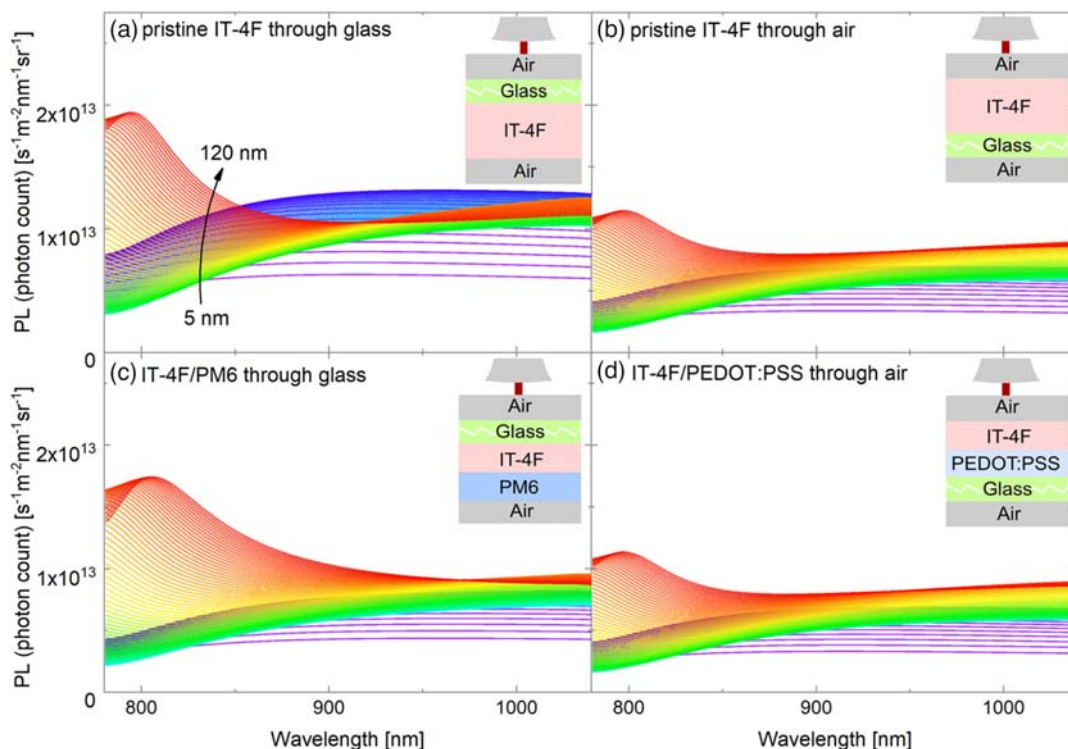
Figure 5. Simulated emission spectra of the different device structures considering an excitation of 1 W m^{-2} at 785 nm (3.951×10^{18} photon s^{-1} m^{-2}) and an emissive layer having (n,k) values of IT-4F but emitting uniformly between 781 and 1040 nm with a quantum efficiency of 3%. The photons are considered emitted from where they are absorbed (see absorption profile in Figure 4). The observed differences come from the differences in absorption of the excitation light and outcoupling of the emitted light. Here the PM6 layer was considered 25 nm thick and the PEDOT:PSS layer 10 nm thick.

to take the effect into account for the PEDOT:PSS samples structures.

For the PM6 quencher samples, however, simulated emissions strongly differ with or without the quencher. As a matter of fact, as shown in Figure S6, Supporting Information, the evolution of QE$^{\mathrm{apparent}}$ strongly resembles the evolution of the experimental PL quenching with the thickness and accounts for most of the observed evolution of quenching for large thicknesses. As a result, the experimental quenching for the PM6 quenching experiment has to be corrected for this optical coupling as follows.

We define a correction factor $\Gamma(\lambda)$ that accounts for the differences in the excitation in-coupling and the emission outcoupling.

$$\Gamma(\lambda) = \frac{\mathrm{PL}_{\mathrm{simulated}}(\lambda)}{\mathrm{PL}_{\mathrm{max}}(\lambda)} \tag{8}$$

where $\mathrm{PL}_{\mathrm{max}}(\lambda) = I_i/W_\lambda$ is the excitation light intensity divided by the width of the simulated spectral range. It accounts for the difference of excited light absorption by the emitting layer and outcoupling of the emitted light.

As shown in **Figure 6**, the uncorrected emission spectra depend a lot on the emitter thickness, due to the fact that the observed emission is not intrinsic to the material but modified by the wavelength-dependent outcoupling. Once corrected, applying this correction factor as $\mathrm{PL}_{\mathrm{corrected}}(\lambda) = \mathrm{PL}_{\mathrm{experimental}}(\lambda)/\Gamma(\lambda)$ becomes much more thickness independent, as shown in Figure 6d.

The evolution of its amplitude with the emitter thickness is also largely changed. The average of the normalized corrected spectra gives the intrinsic emission spectral shape of the emitter.

Finally, we integrated the optical correction $\Gamma(\lambda)$ over the whole spectral range, weighed by the spectral shape of the intrinsic emission; this was done for each emitter thickness, d.

$$\Gamma_{\mathrm{integrated}}(d) = \frac{\sum_{\lambda_i} \Gamma(\lambda_i, d) \times \mathrm{PL}_{\mathrm{corrected}}(\lambda_i, d)}{\sum_{\lambda_i} \mathrm{PL}_{\mathrm{corrected}}(\lambda_i, d)} \tag{9}$$

With this correction at hand, we can calculate the actual PL QE as

$$
\begin{aligned}
\mathrm{QE}^{\mathrm{corrected}}(d) &= 1 - \frac{\mathrm{PL}_{\mathrm{BL}}(d)}{\Gamma_{\mathrm{BL, integrated}}(d)} \times \frac{\Gamma_{\mathrm{emitter, integrated}}(d)}{\mathrm{PL}_{\mathrm{emitter}}(d)} \\
&= 1 - (1 + \mathrm{QE}^{\mathrm{exp}}(d)) \times \frac{\Gamma_{\mathrm{emitter, integrated}}(d)}{\Gamma_{\mathrm{BL, integrated}}(d)}
\end{aligned} \tag{10}
$$

The optical coupling is very sensitive to the PM6 thickness. To account for the uncertainty of the PM6 layer thickness, we simulated different thicknesses within the expected range (24–30 nm). The corrected QE data are presented in **Figure 7**a,b. As can be seen, while the as-measured quenching is very different for both quenchers, the difference decreases significantly after correcting the in- and outcoupling for PM6. This suggests that the corrected QE profiles are more representative of the intrinsic diffusion ability of the NFA excitons. As a result,
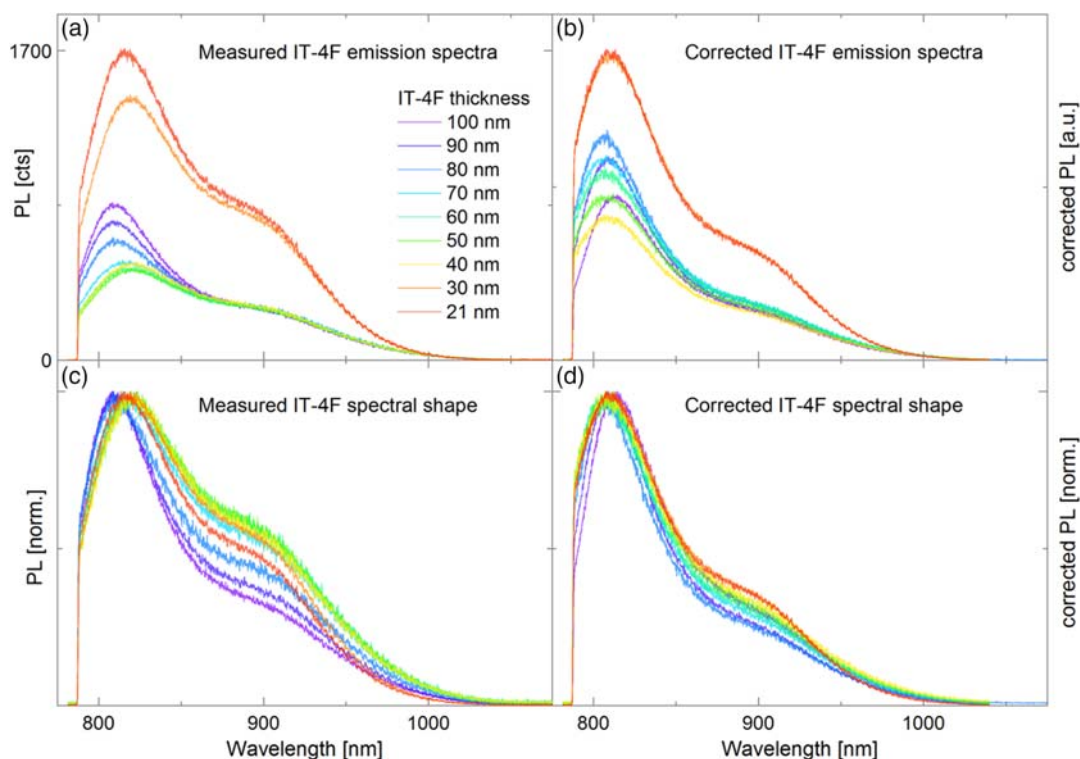
Figure 6. Effect of the in- and outcoupling correction on the IT-4F emission measured from the glass side, without quencher, upon 785 nm excitation for a selection of thicknesses.
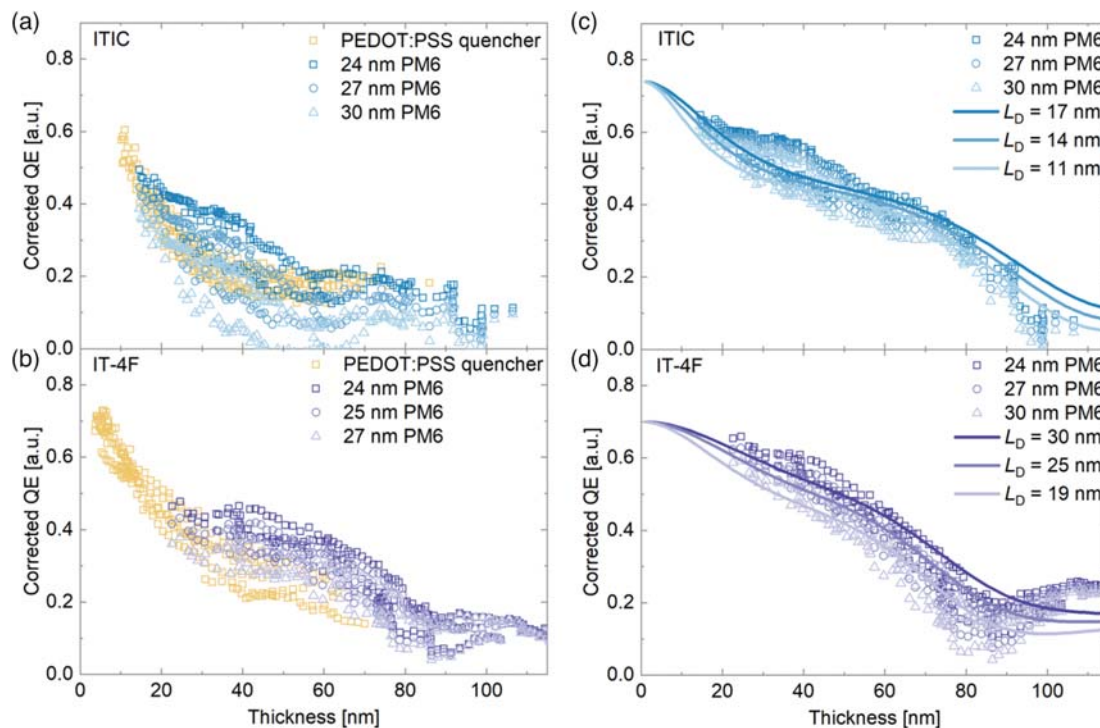
Figure 7. Experimental (scatter) QE curves (785 nm excitation) a,b) corrected for both in- and outcoupling, c,d) corrected only for out-coupling, and modeled (solid curves) QE for the PM6 quencher considering three different PM6 thicknesses for simulation. Only every third data point is shown for clarity.

after correction of the QE, the exciton diffusion lengths extracted from the QE_{PM6} are closer to those found using $QE_{PEDOT:PSS}$ (6–12 nm for ITIC and 8–18 nm for IT-4F) and thus closer to the intrinsic L_d of the NFA material.

The fact that the quenching initially observed in the PM6 quencher systems is an artefact in most of the samples was qualitatively confirmed by transient absorption spectroscopy. Indeed, no significant difference in the exciton lifetime in IT-4F could be observed with or without the PM6 quenching layer for thicknesses between 20 and 60 nm (Figure S7, Supporting Information).

We note that it was not possible to correct the optical coupling effect upon excitation at 633 nm; indeed at that wavelength, a large fraction of the excitation can be absorbed by the PM6. This excitation is then very likely to undergo energy transfer back to the NFA (either via Forster resonant energy transfer or actual photon emission and reabsorption for the thickest films). As a result, the NFA receives more excitation in the bilayer than in the pristine NFA. Applying the outcoupling correction to that experiment reveals it by showing a negative value for the QE, due to the larger emission in the bilayer structure than in the pristine NFA, itself, due to larger excitation (Figure S8, Supporting Information).

Finally, because the fitting Equation (6) used to determine the diffusion length already accounts for the difference in absorption between the different structures, we need to correct only the outcoupling before fitting the data. The separation of the in- and outcoupling effects is detailed in the Supporting Information (Section 10, Figure S9–S11, Supporting Information). The resulting quenching evolution is shown in Figure 7c,d.

For the determination of the diffusion length (vide infra), we considered the whole range of possible couplings, corresponding to the different PM6 thicknesses. The corrected QE profiles correspond to the L_D of 11–17 nm for ITIC and 19–30 nm for IT-4F, respectively. We also note that if the light interference is neglected in the diffusion model (e.g., the simplified Lambert−Beer decay of the electric field intensity is applied), the model fails to adequately describe the QE data, leading to a significant misinterpretation of the L_D (Figure S12, Supporting Information).

2.4. Parameters Controlling the In- and Outcoupling: Design of Quenching Experiments

As we have seen, photoluminescence (PL) quenching using thickness gradient bilayers is a robust tool to determine the exciton diffusion length using a single sample. The use of different quenchers gives comparable results, provided the optical coupling effects are corrected, stressing the fact that we have observed the intrinsic diffusion length of the investigated NFAs. However, the complexity of the data analysis strongly varies between the two chosen quenchers and samples geometries, via the magnitude of the outcoupling correction from negligible (PEDOT:PSS in our case) to critical (PM6).

To aid the design of future experiments, we investigated further the parameters that control this outcoupling efficiency. The idea is to determine the quencher and sample geometry that minimize apparent quenching effect, ideally making the outcoupling

correction unnecessary, as was observed here when using PEDOT:PSS as a quencher. The main differences between our two experiments and hence the main parameters to examine are the quencher's refractive index, its thickness, and the sample geometry.

The light outcoupling effect is associated with a high refractive index at an interface that leads to the formation of optical microcavities or waveguiding effects.[40] To investigate this dependence, we considered a quenching experiment similar to that realized with PM6 as a quencher but with some modified refractive indexes. We simulated the change of PL amplitude solely due to the difference of optical coupling between the regions with and without the quencher, as quantified by the apparent quenching defined in Equation (7). We considered optical indexes such as n_∞ that varies between 1.73 and 2.25, corresponding to the dielectric constant between 3 and 5, typical of a major number of organic materials used in OPV devices, first of all, NFAs.

As shown in Figure S13, S14, Supporting Information, decreasing the refractive index of the quencher decreases the apparent quenching and makes it less dependent on the emitter thickness with the effect being as high as +60–−10% PL amplitude for the largest refractive indexes. However, even when drastically reducing the refractive indexes by simulating a virtual PM6 layer having the refractive index of PEDOT:PSS, the effect remains non-negligible, with some apparent quenching still reaching 20% at low IT-4F thicknesses. Making this correction below 10% could be achieved by decreasing the quencher thickness down to 10 nm. Importantly, both criteria, low refractive index and low quencher thickness, must be met simultaneously to minimize the outcoupling effect. Indeed, a quencher having the refractive index of PM6 but a thickness of 10 nm still results in an optical correction as high as 20% of apparent quenching for the low-emitter thickness. Note also that due to the sensitivity of the outcoupling to the quencher thickness, it is critical to be able to assess that thickness precisely, see Figure 7.

Finally, the position of the emitting layer in a stack, as well as the illumination direction, plays an important role. As intuitively expected, the effects of optical coupling are minimized when reducing the number of layers between the light source and detection and the emitter. This was observed in simulation and confirmed experimentally by illuminating an NFA/PM6 sample in the "normal" measurement geometry from the top (i.e., through the PM6 layer instead of glass); the calculated apparent quenching curve shifts dramatically to the negative direction, as also confirmed experimentally (Figure S15, S16, Supporting Information). However, even in the most favorable case, where the emitter is separated from the detector by only air, the optical correction still increases as high as 30% if a 25 nm PM6 layer is chosen as a quencher.

We also tested the approach on the samples with structurally modified ITIC, which exhibits different optical properties (red- and blueshifts of the absorption spectra) and polycrystalline structures in contrast to as-deposited ITIC and IT-4F (Figure S17, Supporting Information). We observed that these more-crystalline samples exhibit L_D values comparable with the reference samples. For the details see the Supporting Information, Section 14.

3. Conclusion

We present a combined experimental and computational study on the effect of light outcoupling on the determination of the exciton L_D in archetypal NFA materials, ITIC and IT-4F. In this work, a widely applied thickness-dependent interface PL quenching method for probing exciton diffusion was optimized to allow fast, accurate, systematic, and consistent data collection. Two typical OPV materials with very different optical properties were applied as exciton quenchers, PEDOT:PSS and PM6. The L_D estimation based on the measured QE versus NFA layer thickness results in 6–12 nm for ITIC and 8–18 nm for IT-4F in the case of the PEDOT:PSS quencher. The systems with PM6 quencher exhibit dramatically different QE profiles which would correspond to approximately three times larger L_D. Using a computational approach, we demonstrate that, due to the high refractive index of PM6 in contrast to PEDOT:PSS, a contribution of light outcoupling to the output emission is crucial. The correction of the experimental QE profiles results in the estimated L_D values comparable with the PEDOT:PSS systems: 11–17 nm for ITIC and 19–30 nm for IT-4F. We find that apparent quenching due to the difference of outcoupling efficiencies between the emitter alone and bilayer can be minimized by 1) choosing a low-refractive-index quencher, 2) using a thin quencher layer, and 3) using a sample geometry that minimizes the number of interfaces between the emitting layer and the detector. Provided those three conditions are met, the outcoupling correction becomes negligible, thus largely simplifying the data analysis as found for our experiment with the PEDOT:PSS quencher. The fact that, in the study, we apply some of the most common OPV materials underlines the generality of the problem. This raises concerns about the reliability of the pre-existing data obtained by the PL surface quenching method. Consideration of such effects should not be limited only to particular tasks such as L_D or charge transfer energy[40] determination but extended to a broader range of light−matter interaction aspects.[50]

4. Experimental Section

Materials: ITIC (3,9-bis(2-methylene-(3-(1,1-dicyanomethylene)-indanone))-5,5,11,11-tetrakis(4-hexylphenyl)-dithieno[2,3-d:2',3'-d']-s-indaceno[1,2-b:5,6-b']dithiophene, CAS no. 1 664 293-06-4) and IT-4F (3,9-bis(2-methylene-((3-(1,1-dicyanomethylene)-6,7-difluoro)-indanone))-5,5,11,11-tetrakis(4-hexylphenyl)-dithieno[2,3-d:2',3'-d']-s-indaceno[1,2-b:5,6-b']dithiophene or ITIC-4F, CAS no. 2 097 998-59-7) acceptors were purchased from 1-Material, Canada. The donor polymer PM6 (poly[(2,6-(4,8-bis(5-(2-ethylhexyl-3-fluoro)thiophen-2-yl)-benzo[1,2-b:4,5-b']dithiophene))-alt-(5,5-(1',3'-di-2-thienyl-5',7'-bis(2-ethylhexyl)benzo[1',2'-c:4',5'-c']dithiophene-4,8-dione)], CAS no. 1 802 013-83-7; referred to elsewhere in the literature as "PCE135" or "PBDB−T−2F") was purchased from Solarmer, USA. Low-conductivity-grade PEDOT:PSS (poly(3,4-ethyl-enedioxythiophene):polystyrene sulfonate) Clevios P VP. Al 4083 was purchased from Heraeus, Germany. Poly(sodium 4-styrenesulfonate) (molecular weight (MW) $\approx 1 \times 10^6 \, g \, mol^{-1}$) was purchased from Sigma-Aldrich, USA. Standard laboratory-grade solvents (>99.9%) were used throughout. All materials were used as received.

Fabrication of ITIC/PEDOT:PSS Bilayers: Standard microscope glass substrates (76×26 mm) were cleaned by sonication for 15 min in, sequentially, acetone, water/detergent, isopropanol, and NaOH. PEDOT:PSS films (thickness $d \approx 10$ nm) were then deposited in ambient atmosphere from the stock dispersion diluted at 1:1 vol/vol with water by blade coating

at speed = 5 mm s^{-1}, with both substrates and dispersion preheated to 60 °C. Afterward, the edges of the PEDOT:PSS films (width: ≈5–10 mm) along the long substrate axis were removed by brushing with water-soaked tissue, thereby exposing the bare glass substrate, and the obtained films were annealed at 120 °C for 10 min in air. ITIC films were subsequently deposited in nitrogen atmosphere from 0.9 wt% solutions in chloroform by blade coating, with both substrate and solution preheated to ≈60 °C, while IT–4F films were deposited from ≈1.5 wt% solutions in dichloromethane using a preheating temperature of ≈40 °C. In both cases, thickness gradients were generated using a custom-made attachment to continuously vary the coating speed from 99 to 1 mm s^{-1} within a single substrate. This widely employed method[38,39] yielded ITIC and IT-4F films that featured a homogeneous and, essentially, linear ≈1–2 nm mm^{-1} thickness gradient along the coating direction (representative thickness profiles and micrographs are shown in Figure S19, S20, Supporting Information), with the exact value varying somewhat with deposition temperature and blade height.

Fabrication of ITIC/PM6 Bilayers: Given the preferential solubility of ITIC acceptors and PM6 in common solvents, a "floating transfer" method was used for fabricating bilayers that feature a maximally sharp interface. The corresponding processing steps are schematically illustrated in Figure S3, Supporting Information, and described hereafter. On the first set of glass substrates, ITIC and IT-4F films were deposited as described earlier, with films edges (as earlier) subsequently removed using acetone-soaked swabs to obtain ≈12 mm-wide films. On the second set of glass substrates, films of poly(sodium 4-styrenesulfonate) (pNaSS; $d \approx 10$ nm) were spin coated from 1 wt% solution in deionized water (with Triton X-100 surfactant added at ≈1 wt% relative to the amount of solvent). PM6 films (constant thickness: $d \approx 25$ nm) were then deposited atop pNaSS films in nitrogen atmosphere from 0.7 wt% solutions in chlorobenzene by blade-coating at speed = 10 mm s^{-1}, with both substrate and dispersion preheated to 80 °C. Homogeneous PM6/pNaSS bilayer films were thus obtained given the insolubility of pNaSS in solvents other than water. A diamond-tip scribe was then used to create an undercut and define ≈12 mm-wide film regions. Afterward, these films were individually lowered edge first into a Petri dish with water, whereby dissolution of pNaSS detached the hydrophobic PM6 films to float on the water surface and stretched flat by the surface tension of the air−water interface at film edges. A given glass substrate precoated with an ITIC thickness gradient film was then similarly submerged in the same Petri dish and slowly drawn up, hooking the edge of the floating PM6 film onto the ITIC/glass sample to obtain a region along the substrate length in which ITIC and PM6 films overlapped by several mm. Finally, the samples were placed vertically and desiccated to remove the residual water, during which top−down formation of conformal contact was observed for PM6 films with the underlying ITIC or glass surfaces, as apparent from the reflected-light appearance of the films. Hence, the earlier-described floating transfer method yielded bilayer samples that were largely free of defects such as (partial) delamination or folding, as illustrated by the exemplary optical micrographs shown in Figure S21, Supporting Information.

Characterization: NFA gradient thickness profiles were measured by variable-angle spectroscopic ellipsometry (VASE). The ellipsometric functions Ψ and Δ were acquired every 2 mm along a thickness gradient with a GES5E rotating-polarizer ellipsometer (Sopra/Semilab, Hungary) coupled with focusing lenses to reduce the beam size down to ≈0.5 mm in the short axis. The acquired data were fit using the WinElli II software to extract the thickness values. The ellipsometry data were also used to extract the optical indices n and k.

2D PL images were recorded using an alpha300 RA confocal Raman microscope system (WITec GmbH, Germany). Samples were imaged in reflection geometry, with excitation through a 10× objective using two sources: either a 632.8 nm HeNe laser or a 785 nm diode laser. A low laser power (typically 3−12 μW) was used, with no signatures of appreciable semiconductor degradation observed based on PL emission over time. The images were analyzed using WITec Project FIVE software. For the PEDOT:PSS-based samples, excitation and PL collection were made from the top, that is, through air (referred to as "normal geometry"). However, for the PM6-based samples, samples were imaged with excitation/

detection through the glass substrate (referred to as "inverted geometry") to minimize light absorption by the PM6 quencher.

Optical microscopy was performed using a BX51 instrument (Olympus, Japan). Optical absorption spectra were acquired on a VERTEX 70 spectrophotometer with an attached microscope (Bruker, USA). Profile roughness was measured with an Alpha-Step D-500 stylus profilometer (KLA-Tencor, USA).

PESA measurements were performed using a Riken Keiki PESA spectrometer (Model AC-2) with a power setting of 10 nW and a power number of 0.33. Thin-film samples for PESA were prepared on glass substrates.

Supporting Information

Supporting Information is available from the Wiley Online Library or from the author.

Conflict of Interest

The authors declare no conflict of interest.

Data Availability Statement

The data that support the findings of this study are available from the corresponding authors upon reasonable request.

[1] H. Bin, L. Gao, Z.-G. Zhang, Y. Yang, Y. Zhang, C. Zhang, S. Chen, L. Xue, C. Yang, M. Xiao, Y. Li, *Nat. Commun.* **2016**, *7*, 13651.

[2] W. Zhao, S. Li, H. Yao, S. Zhang, Y. Zhang, B. Yang, J. Hou, *J. Am. Chem. Soc.* **2017**, *139*, 7148.

[3] J. Yuan, Y. Zhang, L. Zhou, G. Zhang, H. L. Yip, T. K. Lau, X. Lu, C. Zhu, H. Peng, P. A. Johnson, M. Leclerc, Y. Cao, J. Ulanski, Y. Li, Y. Zou, *Joule* **2019**, *3*, 1140.

[4] Y. Cui, H. Yao, J. Zhang, K. Xian, T. Zhang, L. Hong, Y. Wang, Y. Xu, K. Ma, C. An, C. He, Z. Wei, F. Gao, J. Hou, *Adv. Mater.* **2020**, *32*, 1908205.

[5] Y. Cai, Y. Li, R. Wang, H. Wu, Z. Chen, J. Zhang, Z. Ma, X. Hao, Y. Zhao, C. Zhang, F. Huang, Y. Sun, *Adv. Mater.* **2021**, *33*, 2101733.

[6] M. T. Sajjad, A. Ruseckas, L. K. Jagadamma, Y. Zhang, I. D. W. Samuel, *J. Mater. Chem. A* **2020**, *8*, 15687.

[7] S. Chandrabose, K. Chen, A. J. Barker, J. J. Sutton, S. K. K. Prasad, J. Zhu, J. Zhou, K. C. Gordon, Z. Xie, X. Zhan, J. M. Hodgkiss, *J. Am. Chem. Soc.* **2019**, *141*, 6922.

[8] Y. Firdaus, V. M. Le Corre, S. Karuthedath, W. Liu, A. Markina, W. Huang, S. Chattopadhyay, M. M. Nahid, M. I. Nugraha, Y. Lin, A. Seitkhan, A. Basu, W. Zhang, I. McCulloch, H. Ade, J. Labram, F. Laquai, D. Andrienko, L. J. A. Koster, T. D. Anthopoulos, *Nat. Commun.* **2020**, *11*, 5220.

[9] T. H. Lee, S. Y. Park, W.-W. Park, X. Du, J. H. Son, N. Li, O.-H. Kwon, H. Y. Woo, C. J. Brabec, J. Y. Kim, *ACS Energy Lett.* **2020**, *5*, 1628.

[10] P. A. Hume, W. Jiao, J. M. Hodgkiss, *J. Mater. Chem. C* **2021**, *9*, 1419.

[11] S. M. Menke, W. A. Luhman, R. J. Holmes, *Nat. Mater.* **2013**, *12*, 152.

[12] S. D. Dimitrov, Z. Huang, F. Deledalle, C. B. Nielsen, B. C. Schroeder, R. S. Ashraf, S. Shoaee, I. McCulloch, J. R. Durrant, *Energy Environ. Sci.* **2014**, *7*, 1037.

[13] S. M. Menke, R. J. Holmes, *Energy Environ. Sci.* **2014**, *7*, 499.

[14] A. Serbenta, O. V. Kozlov, G. Portale, P. H. M. van Loosdrecht, M. S. Pshenichnikov, *Sci. Rep.* **2016**, *6*, 36236.

[15] G. J. Hedley, A. Ruseckas, I. D. W. Samuel, *Chem. Rev.* **2017**, *117*, 796.

[16] J. D. A. Lin, O. V. Mikhnenko, J. Chen, Z. Masri, A. Ruseckas, A. Mikhailovsky, R. P. Raab, J. Liu, P. W. M. Blom, M. A. Loi, C. J. García-Cervera, I. D. W. Samuel, T. Q. Nguyen, *Mater. Horiz.* **2014**, *1*, 280.

[17] O. V. Mikhnenko, P. W. M. Blom, T. Q. Nguyen, *Energy Environ. Sci.* **2015**, *8*, 1867.

[18] O. Simpson, *Proc. R. Soc. A* **1957**, *238*, 402.

[19] B. A. Gregg, J. Sprague, M. W. Peterson, *J. Phys. Chem. B* **1997**, *101*, 5362.

[20] A. Haugeneder, M. Neges, C. Kallinger, W. Spirkl, U. Lemmer, J. Feldmann, U. Scherf, E. Harth, A. Gügel, K. Müllen, *Phys. Rev. B* **1999**, *59*, 15346.

[21] M. Theander, A. Yartsev, D. Zigmantas, V. Sundström, *Phys. Rev. B Condens. Matter Mater. Phys.* **2000**, *61*, 12957.

[22] P. Peumans, A. Yakimov, S. R. Forrest, *J. Appl. Phys.* **2003**, *93*, 3693.

[23] W. A. Luhman, R. J. Holmes, *Adv. Funct. Mater.* **2011**, *21*, 764.

[24] A. K. Topczak, T. Roller, B. Engels, W. Brütting, J. Pflaum, *Phys. Rev. B Condens. Matter Mater. Phys.* **2014**, *89*, 201203.

[25] P. E. Shaw, A. Ruseckas, I. D. W. Samuel, *Adv. Mater.* **2008**, *20*, 3516.

[26] B. Siegmund, M. T. Sajjad, J. Widmer, D. Ray, C. Koerner, M. Riede, K. Leo, I. D. W. Samuel, K. Vandewal, *Adv. Mater.* **2017**, *29*, 1604424.

[27] Y. Zhang, M. T. Sajjad, O. Blaszczyk, A. J. Parnell, A. Ruseckas, L. A. Serrano, G. Cooke, I. D. W. Samuel, *Chem. Mater.* **2019**, *31*, 6548.

[28] R. R. Lunt, N. C. Giebink, A. A. Belak, J. B. Benziger, S. R. Forrest, *J. Appl. Phys.* **2009**, *105*, 053711.

[29] K. J. Bergemann, S. R. Forrest, *Appl. Phys. Lett.* **2011**, *99*, 13.

[30] O. V. Mikhnenko, P. W. M. Blom, T. Nguyen, M. Antonietta, *Phys. Chem. Chem. Phys.* **2012**, *14*, 14081 https://doi.org/10.1039/c2cp41359k.

[31] J. D. A. Lin, O. V. Mikhnenko, T. S. Van Der Poll, G. C. Bazan, *Adv. Mater.* **2015**, *27*, 2528.

[32] B. A. L. Raul, Y. N. Luponosov, W. Yang, N. M. Surin, O. Douhéret, J. Min, T. L. C. Jansen, S. A. Ponomarenko, M. S. Pshenichnikov, *Sci. Rep.* **2020**, *10*, 1.

[33] L. A. A. Pettersson, L. S. Roman, O. Inganäs, *J. Appl. Phys.* **1999**, *86*, 487.

[34] T. Stübinger, W. Brütting, *J. Appl. Phys.* **2001**, *90*, 3632.

[35] J. J. M. Halls, K. Pichler, R. H. Friend, *J. Appl. Phys.* **1996**, *68*, 3120.

[36] V. Bulović, S. R. Forrest, *Chem. Phys.* **1996**, *210*, 13.

[37] D. Qin, P. Gu, R. S. Dhar, S. G. Razavipour, D. Ban, *Phys. Status Solidi Appl. Mater. Sci.* **2011**, *208*, 1967.

[38] C. M. Stafford, K. E. Roskov, T. H. Epps, M. J. Fasolka, *Rev. Sci. Instrum.* **2006**, *77*, 023908.

[39] A. Sánchez-Díaz, X. Rodríguez-Martínez, L. Córcoles-Guija, G. Mora-Martín, M. Campoy-Quiles, *Adv. Electron. Mater.* **2018**, *4*, 1700477.

[40] M. List, T. Sarkar, P. Perkhun, J. Ackermann, C. Luo, U. Würfel, *Nat. Commun.* **2018**, *9*, 3631.

[41] R. Kerremans, C. Kaiser, W. Li, N. Zarrabi, P. Meredith, A. Armin, *Adv. Optical Mater.* **2020**, *8*, 2000319 https://doi.org/10.1002/adom.202000319.

[42] E. Pascual-San-José, X. Rodríguez-Martínez, R. Adel-Abdelaleim, M. Stella, E. Martínez-Ferrero, M. Campoy-Quiles, *J. Mater. Chem. A* **2019**, *7*, 20369.

[43] A. Van Dijken, A. Perro, E. A. Meulenkamp, K. Brunner, *Organic Electronics* **2003**, *4*, 131 https://doi.org/10.1016/j.orgel.2003.08.007.

[44] A. Elschner, S. Kirchmeyer, W. Lövenich, U. Merker, K. Reuter, *PEDOT Principles and Applications of an Intrinsically Conductive Polymer*, CRC Press Taylor & Francis Group, Boca Raton **2011**.

[45] D. Abbaszadeh, G. A. H. Wetzelaer, H. T. Nicolai, P. W. M. Blom, *J. Appl. Phys.* **2014**, *116*, 224508.

[46] Y. Wang, Q. Fan, X. Guo, W. Li, B. Guo, W. Su, X. Ou, M. Zhang, *J. Mater. Chem. A* **2017**, *5*, 22180.

[47] Q. Fan, W. Su, Y. Wang, B. Guo, Y. Jiang, X. Guo, F. Liu, T. P. Russell, M. Zhang, Y. Li, *Sci. China Chem.* **2018**, *61*, 531.

[48] G. F. Burkhard, E. T. Hoke, M. D. McGehee, *Adv. Mater.* **2010**, *22*, 3293.

[49] P. Yeh, *Optical Waves in Layered Media*, Wiley, Hoboken, NJ, USA **2005**.

[50] A. Lewandowska-Andralojc, B. Marciniak, *ACS Energy Lett.* **2019**, *4*, 1898.